

Article

MXene/NiO Composites for Chemiresistive-Type Room Temperature Formaldehyde Sensor

Baoyu Huang¹, Xinwei Tong¹, Xiangpeng Zhang², Qiuxia Feng³, Marina N. Rumyantseva⁴ , Jai Prakash⁵ 
and Xiaogan Li^{1,*}

¹ School of Microelectronics, Dalian University of Technology, Dalian 116024, China; huangby@dlut.edu.cn (B.H.)

² AVIC Jonhon Optron Technology Co., Ltd., Luoyang 471003, China

³ School of Information and Control Engineering, Qingdao University of Technology, Qingdao 266520, China

⁴ Laboratory of Chemistry and Physics of Semiconductor and Sensor Materials, Chemistry Department, Moscow State University, Leninskie Gory 1-3, Moscow 199991, Russia

⁵ Department of Chemistry, National Institute of Technology (NIT), Hamirpur 177005, India

* Correspondence: lixg@dlut.edu.cn

Abstract: In this work, MXene/NiO-composite-based formaldehyde (HCHO) sensing materials were successfully synthesized by an in situ precipitation method. The heterostructures between the MXene and NiO nanoparticles were verified by transmission electron microscopy (TEM), X-ray diffraction (XRD), and X-ray photoelectron spectroscopy (XPS). The HCHO sensing performance of the MXene/NiO-based chemiresistive-type sensors was investigated. Compared to pure MXene and NiO materials, the sensing performance of the MXene/NiO-P2-based sensor to HCHO gas at room temperature was significantly enhanced by the formation of MXene/NiO heterojunctions. The response of the MXene/NiO-P2 sensor to 50 ppm HCHO gas was 8.8, which was much higher than that of the pure MXene and NiO. At room temperature, the detectable HCHO concentration of the MXene/NiO-P2-based sensor was 1 ppm, and the response and recovery time to 2 ppm HCHO was 279 s and 346 s, respectively. The MXene/NiO-P2 sensor also exhibited a good selectivity and a long-term stability to HCHO gas for 56 days. The in situ Fourier transform infrared (FTIR) spectra of the MXene/NiO-P2 sensor, when exposed to HCHO gas at different times, were investigated to verify the adsorption reaction products of HCHO molecules.

Keywords: chemiresistive-type formaldehyde sensor; MXene/NiO; heterojunctions; room temperature



check for updates

Citation: Huang, B.; Tong, X.; Zhang, X.; Feng, Q.; Rumyantseva, M.N.; Prakash, J.; Li, X. MXene/NiO Composites for Chemiresistive-Type Room Temperature Formaldehyde Sensor. *Chemosensors* **2023**, *11*, 258. <https://doi.org/10.3390/chemosensors11040258>

Academic Editor: Vardan Galstyan

Received: 13 February 2023

Revised: 16 April 2023

Accepted: 19 April 2023

Published: 21 April 2023



Copyright: © 2023 by the authors. Licensee MDPI, Basel, Switzerland. This article is an open access article distributed under the terms and conditions of the Creative Commons Attribution (CC BY) license (<https://creativecommons.org/licenses/by/4.0/>).

1. Introduction

Formaldehyde (HCHO) is a highly toxic volatile organic compound (VOC) gas. It is mainly obtained from manufacturing and building decoration materials. Formaldehyde is also recognized as one of the most serious pollutants and carcinogenic VOC gases in indoor and urban environments [1,2]. Formaldehyde can react in the upper respiratory tract of people's eyes, noses, and can cause throat irritation resulting in throat discomfort, headache, nausea, etc. Direct exposure to excessive formaldehyde gas may also damage the human central nervous system, causing immune system disorder, and can seriously threaten human health [3,4]. Therefore, it is necessary to develop a portable sensor that can quickly and accurately identify formaldehyde gas in the environment.

Chemiresistive-type gas sensors based on metal oxide semiconductors have been widely studied during the last few decades, due to their high response, long-term stability, and low cost. However, the traditional metal oxide gas sensors usually work at a high temperature (150–400 °C), which introduces a problem of high energy consumption, greatly limiting the intelligent and integrated process of the gas sensors. To meet the low power consumption requirements of portable formaldehyde sensors, there is an urgent need to develop new sensing materials that can work at room temperatures. Two-dimensional (2D)

nanomaterials such as graphene [5], reduced graphene oxide (rGO) [6], black phosphorus (BP) [7], transition metal disulfides (TMDs) [8], and MXene [9] have attracted great interest in the field of room temperature gas sensing materials, due to their excellent gas adsorption capacity, which is due to their unique microstructures. Among them, MXene not only has the characteristics of a high specific surface area and high conductivity similar to graphene, black phosphorus, and other two-dimensional materials, but it also has the advantages of adjustable chemical composition, controllable nanolayer structure, and abundant functional groups on the surface, which allows it further to exhibit excellent chemical reactivity and hydrophilicity [10–14]. MXene refers to a large family of two-dimensional (2D) transition metal carbides, nitrides, and carbonitrides [10,15]. $\text{Ti}_3\text{C}_2\text{T}_x$ is one of the most widely used and well-studied examples of MXene. $\text{Ti}_3\text{C}_2\text{T}_x$ MXene is obtained by selectively etching Al from its MAX phase with HF, where T_x represents various surface functional groups such as -OH, -O, -F, etc. These functional groups can provide abundant active sites for gas adsorption on the surface of MXene. Previous studies have showed that MXene has obvious responses to several VOC gases (including acetone, ethanol, and ammonia) at room temperatures, further confirming its application prospects in the field of room temperature gas sensors [16]. However, the pure MXene-based sensors still suffer from low response and poor selectivity. To improve the sensing performance, the modification of MXene with metal oxide nanocrystals has been investigated [14,17–19]. Zhang et al. reported the utilization of a room temperature formaldehyde sensor that used a MXene/ Co_3O_4 composite [14]. He et al. reported that an MXene/ SnO_2 heterojunction-based sensor had excellent sensitivity and selectivity to NH_3 at room temperatures [17]; the improved sensing properties were proposed to be attributed to the formation of the heterojunctions between MXene and the metal oxide [14,17].

NiO is a typical p-type semiconductor with a band gap of 3.6–4.0 eV. In the past few years, NiO with different morphologies and nanostructures have been widely used in gas sensing [20–23]. A gas sensor based on the flower-like NiO prepared by San et al. showed a high response and good selectivity to formaldehyde gas at 200 °C [20]. Hu et al. reported the use of a hollow NiO sphere-polyaniline-composite-based gas sensor. Due to the hollow structure and the formation of p-p heterojunctions, the sensor displayed a good sensing performance to NH_3 gas at room temperature [23]. Therefore, constructing MXene/NiO heterojunction materials is considered to be a feasible design scheme to realize the detection of formaldehyde gas at room temperatures.

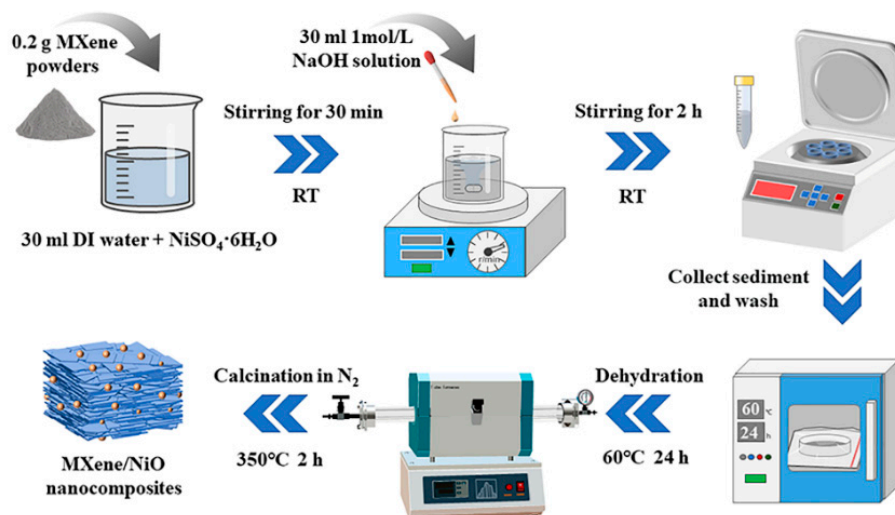
In this paper, MXene/NiO composites were synthesized by an in situ precipitation method. The prepared MXene/NiO-based chemiresistive-type sensor showed an excellent sensing performance at detecting formaldehyde gas at room temperature. In particular, the sensor based on MXene/NiO-P2 composite materials exhibited much higher sensitivity, selectivity, and long-term stability to formaldehyde gas at room temperatures than those of pure MXene materials, showing a promising prospect for formaldehyde detection at low temperatures.

2. Experimental Section

2.1. Synthesis of MXene/NiO Composites

All chemical reagents used in this work were analysis grade without further purification. The $\text{Ti}_3\text{C}_2\text{T}_x$ MXene was purchased from Laizhou Kai Xi Ceramic Materials Co., Ltd. (Yantai, China). The $\text{NiSO}_4 \cdot 6\text{H}_2\text{O}$ and NaOH were of analysis grade and were purchased from Aladdin Chemical Reagents. The chemical preparation process of MXene/NiO is shown in Scheme 1. Firstly, 384 mg, 512 mg, and 768 mg $\text{NiSO}_4 \cdot 6\text{H}_2\text{O}$ were, respectively, added into 30 mL deionized water to prepare three different concentrations of NiSO_4 solutions. Secondly, 200 mg MXene was then added to the above prepared NiSO_4 solutions to obtain uniform suspension by stirring for 0.5 h at room temperature (RT), and then a 30 mL 1 mol/L NaOH aqueous solution was dropped into the solution. After being stirred for 2 h, the precipitates were collected and washed three times with deionized water and three times with ethanol. Then, the samples were dried at 60 °C for 24 h. Finally, the MXene/NiO

composite materials were obtained after being calcined at 350 °C for 2 h under N₂, which were denoted as MXene/NiO-P1, MXene/NiO-P2, and MXene/NiO-P3. Furthermore, the pure NiO was also prepared for comparison purposes. Firstly, Ni(NO₃)₂·6H₂O was added into the deionized water to prepare Ni(NO₃)₂ solutions. Then, the solution was transferred into a Teflon-lined autoclave and maintained at 180 °C for 12 h. Finally, the precipitate, after washing by deionized water and ethanol, was annealed at 400 °C for 4 h to obtain NiO material.



Scheme 1. Chemical preparation process of the MXene/NiO materials.

2.2. Characterization

The crystalline structures of the materials were measured by X-ray diffraction (XRD: Bruker D8 Advance, Mannheim, Germany) using Cu K α 1 radiation ($\lambda = 0.15406$ nm) in the range of 5° to 90°. The surface morphologies and microstructure of the samples were characterized by using scanning electron microscopy (SEM: Regulus8100, Hitachi, Tokyo, Japan) and transmission electron microscopy (TEM: Tecnai G2 F30, FEI, Hillsboro, OR, USA). X-ray photoelectron spectroscopy (XPS: ESCALAB 250Xi, The Semel fisher technologies, Boca Raton, FL, USA) with an Al K α radiation source ($h\nu = 1486.6$ eV) were used to analyze the surface elemental composition of the materials. The Fourier transform infrared (FTIR) spectra were characterized by an FTIR spectrometer (The Semel fisher Nicolet iS5, Boca Raton, FL, USA), which was used to verify the adsorbed species on the surface of the sensing materials.

2.3. Sensor Fabrication and Electrical Measures

As shown in Figure S1a, the prepared MXene/NiO composite powders were added to an agate mortar, and then 4–5 drops of deionized water was added to it. After grinding for 10 min, a uniform paste was obtained, which was evenly dropped onto the interdigitated electrodes. Finally, the interdigitated electrodes coated with the sensing materials were dried in an oven at 60 °C for 12 h to obtain the sensor based on MXene/NiO composites (Figure S1b). As shown in Figure S1c, the sensing measurements were performed in a static gas sensing test system with a total capacity of 50 L, which was equipped with a digital multimeter (Keysight 34465A), DC power supply (KEYSIGHT E36311A), as well as an evaporation platform and computer. After the resistance of the sensor was stabilized in air, different volumes of the calculated target liquid were injected into the closed chamber with micro syringes. A specific concentration of the VOC gas testing environment was created by vaporizing the corresponding liquid. The resistances of the sensors were directly

measured by a digital multimeter. The response of the sensor was defined as the resistance of the sensor in the target gas divided by that in air, as shown in reaction (1).

$$S = \frac{R_g}{R_a} \quad (1)$$

Here, R_a is the resistance in air and R_g is the resistance in the target gas. Response time (T_{res}) is defined as the time that it takes for the sensor to reach 90% of the change in its stable resistance after being exposed to the measured gas. The recovery time (T_{rec}) is defined as the time taken by the sensors to achieve 90% of the total resistance change in the case of desorption of the tested gas.

3. Results and Discussion

3.1. Characterization of Sensing Materials

Figure 1a,b show the SEM images of the MXene and MXene/NiO-P2 materials, respectively. It can be seen that MXene presents an obvious lamellar structure with a flat and smooth surface. As shown in Figure 1b, after becoming a composite with NiO, the surface of the MXene/NiO-P2 material becomes obviously rough. Some NiO nanoparticles are covered on the surface of MXene, and some are randomly embedded in MXene layers. The SEM images of MXene/NiO-P1 and MXene/NiO-P3 are shown in Figure S2. It can be noticed that the NiO nanoparticles are also randomly distributed on the surface and the interlayer of the MXene material. The TEM images (Figure 1c,d) of MXene/NiO-P2 further clearly display that there are some nanoparticles attached to the thin and transparent MXene sheets, which should be NiO nanoparticles. A high-resolution TEM (HRTEM) image of the MXene/NiO-P2 composite is shown in Figure 1e, where clear lattice fringes and grain boundaries between the NiO nanoparticle and MXene can be seen. The 0.20 nm lattice spacing measured from the image is consistent with the (200) crystal plane spacing of cubic NiO. In addition, the lattice spacing of 0.25 nm corresponds to the (006) crystal plane of MXene [24]. Figure 1f shows the corresponding selected area electron diffraction (SAED) pattern of MXene/NiO-P2, in which the three diffraction lines in the innermost circle correspond to the crystal planes ((111), (200), and (220) of NiO, respectively). Figure 1g–j further exhibit the element mapping images of the MXene/NiO-P2 sample. The C, Ti, O, and Ni elements are evenly distributed in the sample, indicating that the NiO nanoparticles were uniformly modified on the surface of the MXene.

To investigate the crystallographic information and phase composition of the materials, the XRD patterns of MXene, NiO, and MXene/NiO-P2 samples were obtained, and are displayed in Figure 2. All of the diffraction peaks of NiO matched well with the NiO bunsenite phase (JCPDS card NO.47-1049), and the characteristic peaks located at 37.2°, 43.3°, 62.9°, 75.4°, and 79.4° corresponded to the (111), (200), (220), (311), and (222) lattice planes of NiO, respectively. The characteristic peaks of pristine MXene were located at the 2θ of 9.1°, 18.3°, 27.5°, 34.5°, 36.8°, 40.9°, and 60.7°, which are related to the (002), (004), (006), (0010), (103), (0012), and (110) lattice planes of MXene, respectively [25,26]. The (0010), (103), (0012), and (110) peaks contributed to the –OH-terminated surface group, which is consistent with previous literature reports [27]. For the MXene/NiO-P2 composites, the characteristic peaks all corresponded to MXene and NiO, indicating the successful synthesis of the MXene/NiO-P2 nanocomposites. In addition, compared with the pristine MXene, the (002) peak of MXene/NiO-P2 shifted to the lower angle, which can be attributed to the intercalating of NiO among the interlayers of MXene [28].

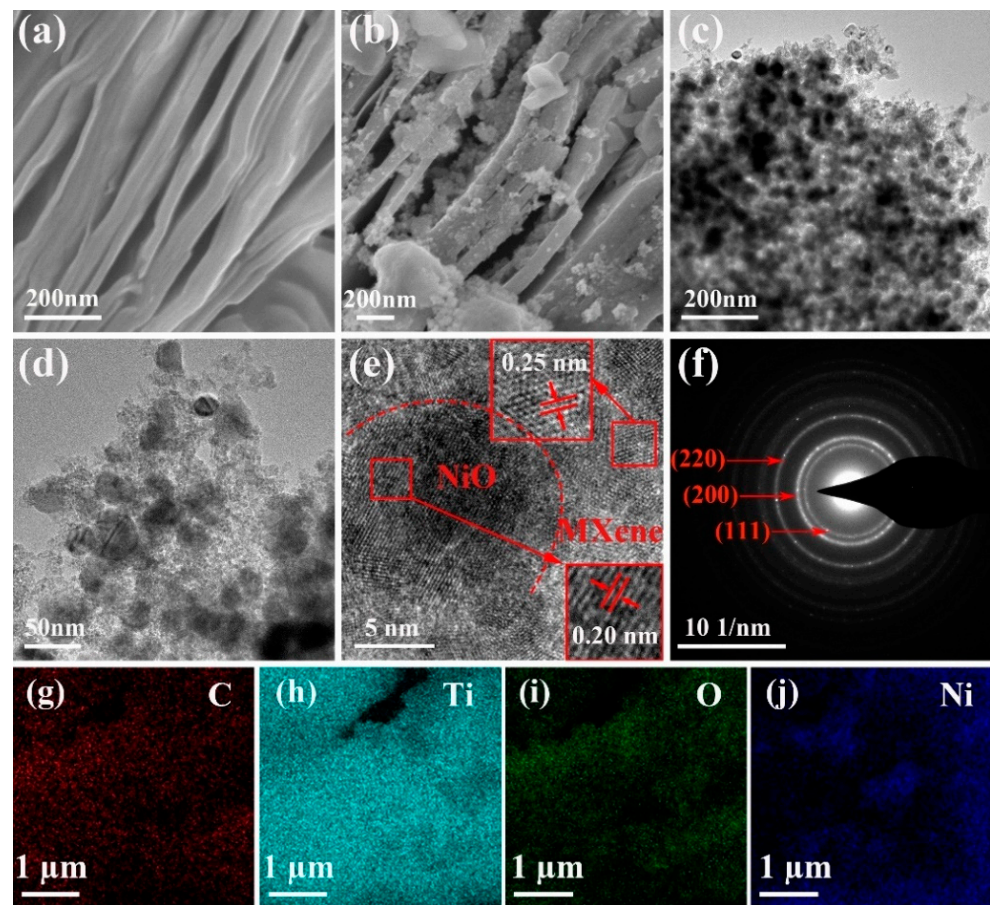


Figure 1. SEM images of (a) MXene and (b) MXene/NiO-P2. (c,d) TEM images of MXene/NiO-P2. (e) HRTEM micrograph of MXene/NiO-P2. (f) SAED pattern of MXene/NiO-P2. (g–j) EDS elemental mapping images of MXene/NiO-P2.

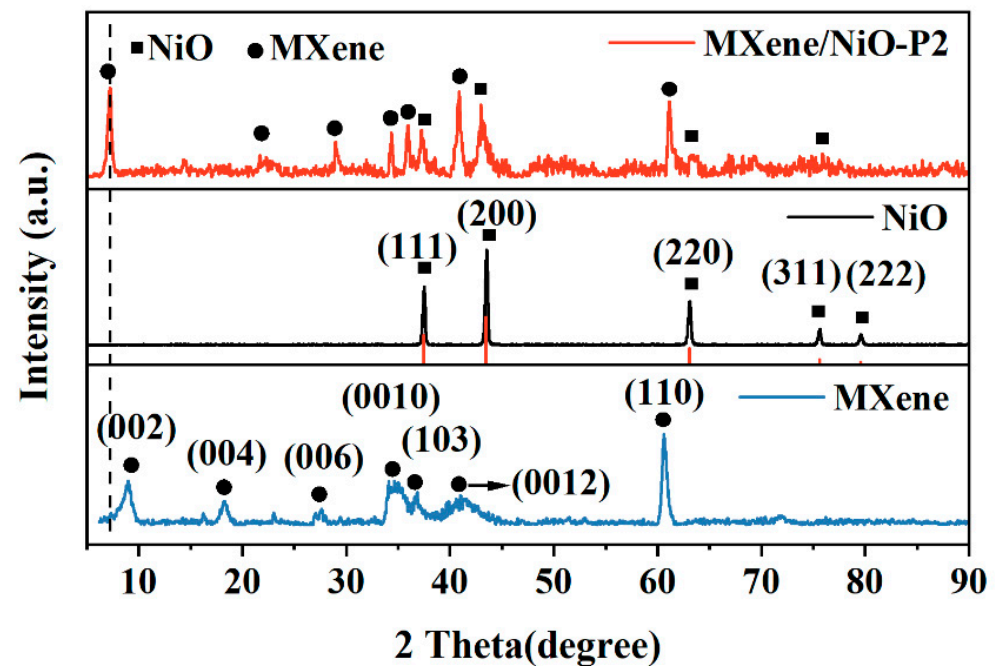


Figure 2. XRD patterns of MXene, NiO, and MXene/NiO-P2.

To further explore the chemical composition and bonding state of the materials, the XPS spectra of pristine MXene and MXene/NiO-P2 composites were obtained, and are exhibited in Figure 3a–f. Figure 3a shows the survey spectra of MXene and MXene/NiO-P2. The peaks of C, Ti, O, and F elements could be observed in MXene. For the MXene/NiO-P2 composites, the peaks corresponding to the C, Ti, O, F, and Ni elements could be found, indicating the existence of NiO in the composites [20,29]. The existence of the F element in MXene may be caused by the introduction of LiF in the etching process. Compared with MXene, the signal intensity of F in the MXene/NiO-P2 material was greatly reduced, indicating that a large amount of F[−] can be removed from the surface of MXene during the preparation process. In Figure 3b, the two peaks of Ni 2p_{3/2} and Ni 2p_{1/2} located at 855.5 eV and 873.4 eV corresponded to the typical Ni-O bonds of NiO, confirming the existence of NiO in the MXene/NiO-P2 composites. The peaks with the binding energies of 861.6 eV and 880.1 eV belonged to the shake-up satellite peaks ascribed to the Ni 2p_{3/2} and Ni 2p_{1/2}, respectively [30]. The Ti 2p spectra of the MXene and MXene/NiO-P2 are shown in Figure 3c,d. The two peaks positioned at 455.3 eV and 459.7 eV were assigned to Ti 2p_{3/2} and Ti 2p_{1/2} of the Ti-C bond [12]. The peaks located at 457.2 eV and 462.9 eV were assigned to the 2p_{3/2} and 2p_{1/2} orbits of Ti³⁺ in Ti₃C₂T_x MXene, and the peaks at 455.8 eV and 461.5 eV were attributed to the 2p_{3/2} and 2p_{1/2} orbits of Ti²⁺ [31]. Compared with pure MXene, the peak of Ti³⁺ in the MXene/NiO-P2 composites moved toward a higher binding energy; this was due to the loss of electrons, which indicates the formation of the MXene/NiO heterojunction [32,33]. Figure 3e shows the C1s' characteristic spectrum of MXene/NiO-P2, which is equipped with four peaks at 282.0 eV, 284.8 eV, 286.3 eV, and 288.6 eV, which correspond to C-Ti, C-C, C-O, and C=O, respectively [34]. Additionally, the O1s spectra of MXene/NiO-P2 is seen in Figure 3f. The peaks located at 529.8 eV and 531.3 eV were attributed to the lattice oxygen (O_{lat}) of NiO and the adsorbed oxygen (O_{ads}), respectively. In fact, surface-adsorbed oxygen was critical for the sensing materials since the target gas interacted with them, giving sensitivity.

FTIR characterization is an effective means by which to understand the types of chemical bonds in materials. As shown in Figure 4, the dips at 3458 cm^{−1} and 2924 cm^{−1} correspond to hydroxyl groups. The dip at 1635 cm^{−1} directly demonstrates the presence of the C=O functional groups. For the NiO sample, the C=O bond may be assigned to the adsorption of atmospheric CO₂. The dips positioned at 1381 cm^{−1} and 1148 cm^{−1} belong to the O-H and C-O functional groups, which are consistent with the result of XPS [35]. The dips at 820 cm^{−1} and 545 cm^{−1} were attributed to C-H deformation vibrations and Ti-OH, respectively [36,37]. The dip at 445 cm^{−1} was associated to the Ni-O bonds [38]. According to the FTIR data, it can be concluded that the surface of MXene/NiO-P2 is rich in hydroxyl and other oxygen-containing functional groups, which is conducive to the improvement of gas sensing properties.

3.2. Electrical and Sensing Properties of Gas Sensors

Figure 5 shows the I-V curves of sensors based on MXene/NiO-P2, pure NiO, and pure MXene in the voltage ranging from −5 V to +5 V. For the MXene/NiO-P2- and MXene-based sensors, the voltage and current showed a linear relationship, which confirmed the ohmic contact between the sensing material and the electrode. The larger slope of the I-V curve indicates that MXene has a very low resistance due to its excellent metallic properties. Moreover, as is shown in Figure 5, a NiO sensor exhibits a high resistance at room temperature, with the slope of its I-V curve being almost zero.

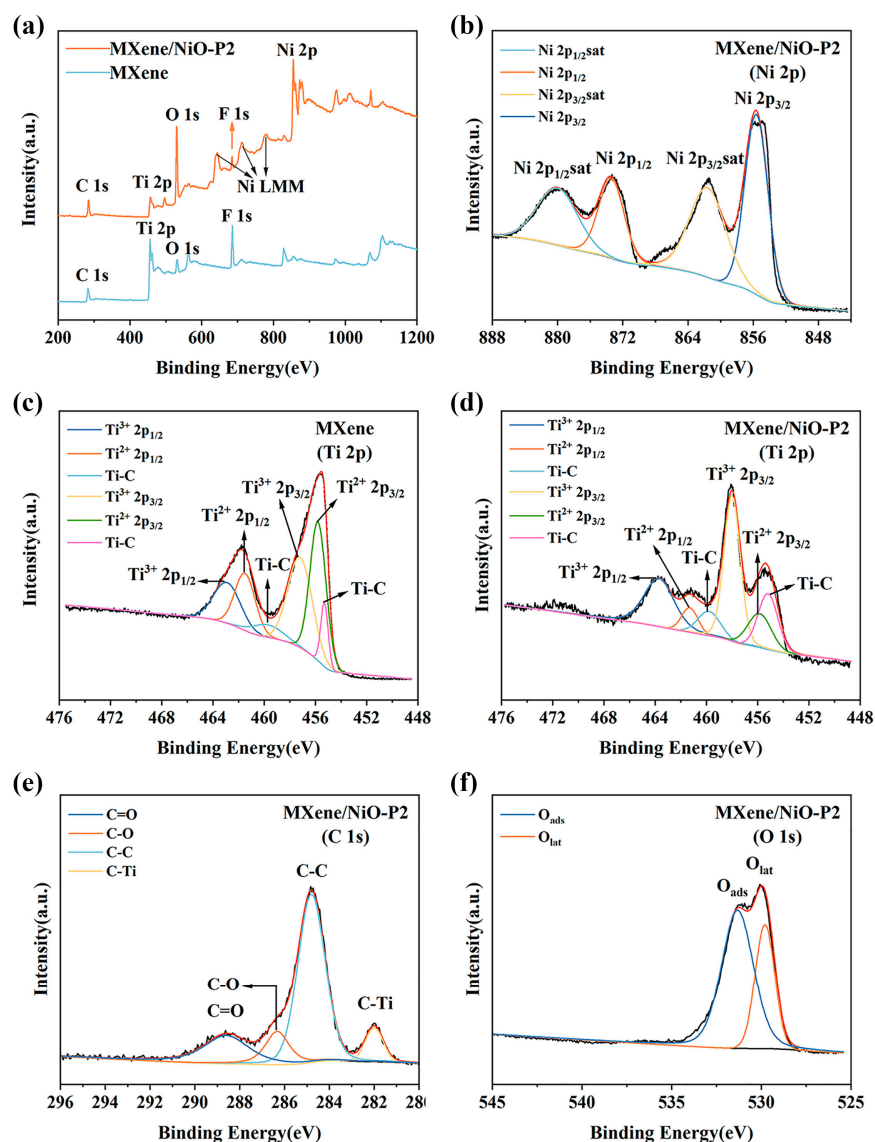


Figure 3. (a) The XPS survey spectra of MXene and MXene/NiO-P2; (b) the Ni 2p spectrum of MXene/NiO-P2; and (c,d) the Ti 2p spectra of MXene and MXene/NiO-P2, respectively. (e) The C1s spectrum and (f) O1s spectrum of MXene/NiO-P2.

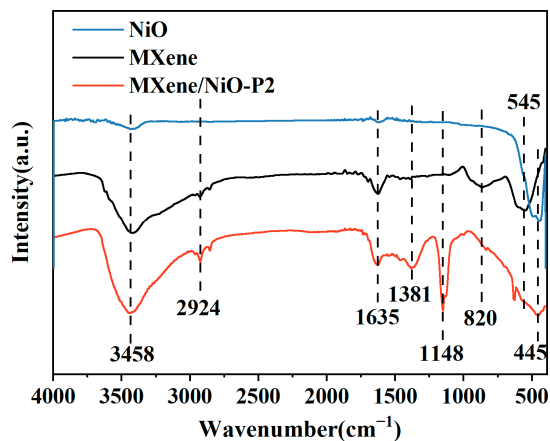


Figure 4. FTIR spectra of MXene, NiO, and MXene/NiO-P2.

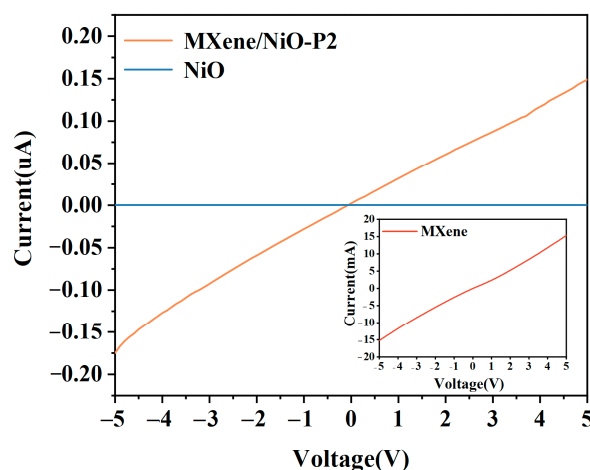


Figure 5. I-V curves of the sensors based on MXene/NiO-P2, NiO, and MXene.

The real-time resistance changes in the MXene/NiO-P2-based chemiresistive-type sensor to 10–100 ppm HCHO at 25 °C and RH = 40% is shown in Figure 6a. When the sensor was exposed to reductive HCHO gas, the resistance of the sensor rose sharply. When the sensor was re-exposed to air, the resistance of the sensor immediately dropped back to the previous resistance value. The MXene/NiO-P2 sensor exhibited a typical p-type sensing behavior. The real-time resistance change curves of MXene/NiO-P1- and MXene/NiO-P3-based chemiresistive-type sensors are also shown in Figure S3. It can be seen that with the increase in NiO incorporation, the baseline resistance of the MXene/NiO composites presented a gradually increasing trend; this was due to the high resistance of NiO, which was consistent with the results of the I-V curves. Figure 6b shows the response curves of the three MXene/NiO chemiresistive-type sensors. The response amplitude gradually increased as the concentration of HCHO increased from 10 ppm to 100 ppm. Moreover, it can be noticed that the MXene/NiO-P2 sensor displayed the highest response to HCHO, and its response value to 100 ppm HCHO gas was 13.61 (R_g/R_a). Furthermore, it should be mentioned that to exclude the effect of heat treatment during the preparation process on the sensing properties of MXene, the sample of MXene-350C was obtained by calcining the pristine MXene at 350 °C for 2 h under N₂. As shown in Figure S4, the response of the sensor based on MXene-350C to a concentration of 10–100 ppm HCHO at 25 °C was extremely weak and almost negligible compared to MXene/NiO-P2. Therefore, the improved response performance of MXene/NiO-P2 should be attributed to the formation of the heterojunction. It is necessary to further explore the sensing performance of an MXene/NiO-P2-based sensor to low concentrations of HCHO. As shown in Figure 6c, the MXene/NiO-P2 sensor exhibits obvious response and excellent response/recovery properties to 1–8 ppm HCHO at room temperature. The response and recovery times of the MXene/NiO-P2 sensor to 2 ppm HCHO were 279 s and 346 s, respectively, as is shown in the inset in Figure 6c. Furthermore, according to the standard given by the National Institute of Occupational Safety and Health (NIOSH) and the World Health Organization (WHO), the allowable limits of formaldehyde in the environment are 1 ppm and 0.08 ppm, respectively [39]. Therefore, the limit of detection (1 ppm) of the prepared formaldehyde sensor needs to be further enhanced. In the future work, noble metals (Au, Pt, Pd, etc.) and TiO₂, which has excellent sensing performance to formaldehyde gas, will be considered to modify the prepared sensing material in order to further improve the limit of detection (LOD) of the formaldehyde sensor [40,41]. Moreover, using UV irradiation technology to optimize the LOD of the sensor is also worth studying in future work [42]. The fitting curve of the sensor response to 1–100 ppm HCHO is shown in Figure 6d. The response of the MXene/NiO-P2 sensor displayed an approximately linear relationship with HCHO concentration.

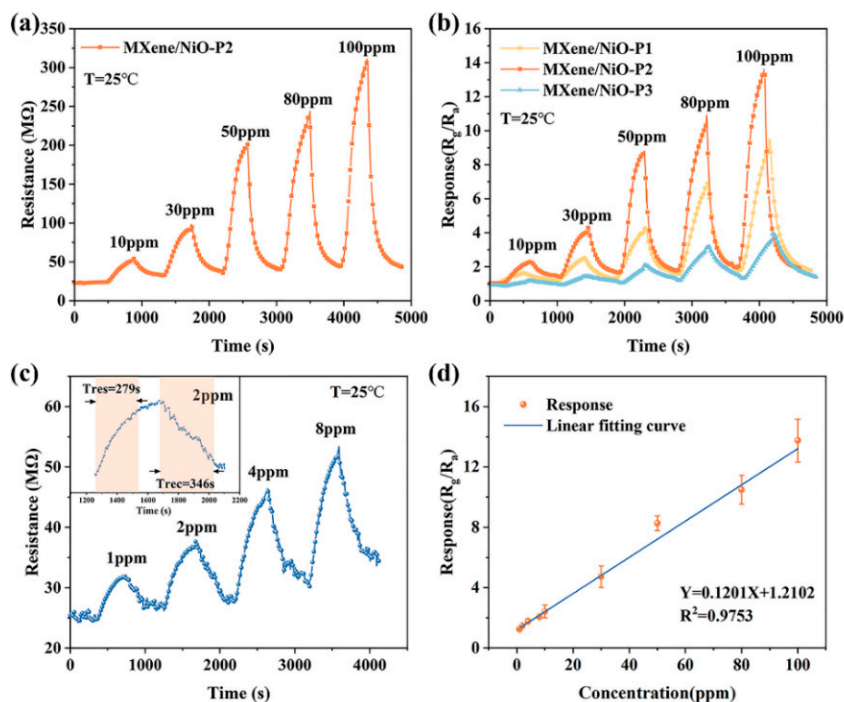


Figure 6. (a) Real-time resistance changes in the sensors based on MXene/NiO-P2 to 10–100 ppm HCHO at 25 °C. (b) Response changes in the sensors based on MXene/NiO-P1, MXene/NiO-P2, and MXene/NiO-P3 to 10–100 ppm HCHO at 25 °C. (c) Real-time resistance changes in the MXene/NiO-P2 sensor to the low concentrations (1–8 ppm) of HCHO at 25 °C. (d) The response fitting curves of the MXene/NiO-P2 sensor to 1–100 ppm HCHO at 25 °C.

Figure 7 shows the response curves of NiO, MXene, and MXene/NiO-P2 sensors to 10–100 ppm HCHO at room temperature. It can be seen that there is no obvious response from the pure NiO and pure MXene sensors to HCHO gas. However, the MXene/NiO-P2 sensor displayed a high response to HCHO at room temperature, indicating that the construction of MXene/NiO heterojunctions is the main factor by which to enhance the sensing performance to HCHO at room temperatures.

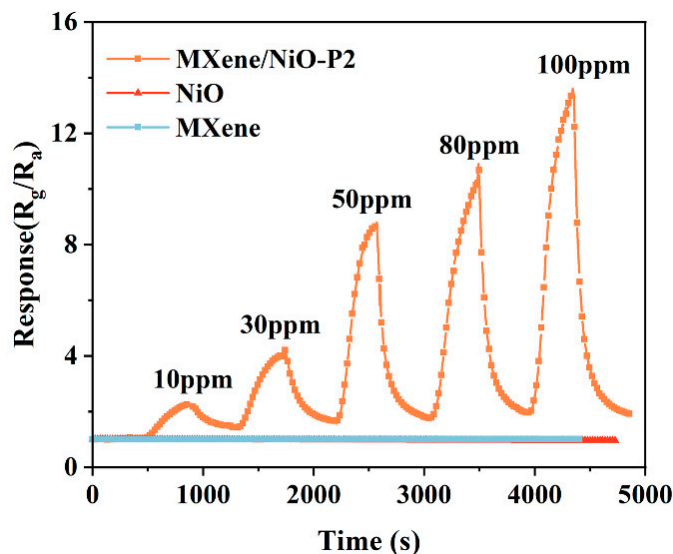


Figure 7. Response changes in the sensors based on MXene/NiO-P2, MXene, and NiO to 10–100 ppm HCHO at 25 °C.

To further investigate its sensing performance, the response curves of the MXene/NiO-P2 sensor to 10 ppm HCHO were measured at different operating temperatures (25–80 °C), and are shown in Figure 8a. As the temperature increased from 25 °C to 80 °C, the response of the MXene/NiO-P2 sensor to 10 ppm HCHO gradually decreased, indicating that room temperature (25 °C) is the optimum working temperature for the sensor. This may be related to the fact that a higher working temperature can accelerate the desorption of the gas molecules from the surface of the sensing material, thus leading to a decreased response [43].

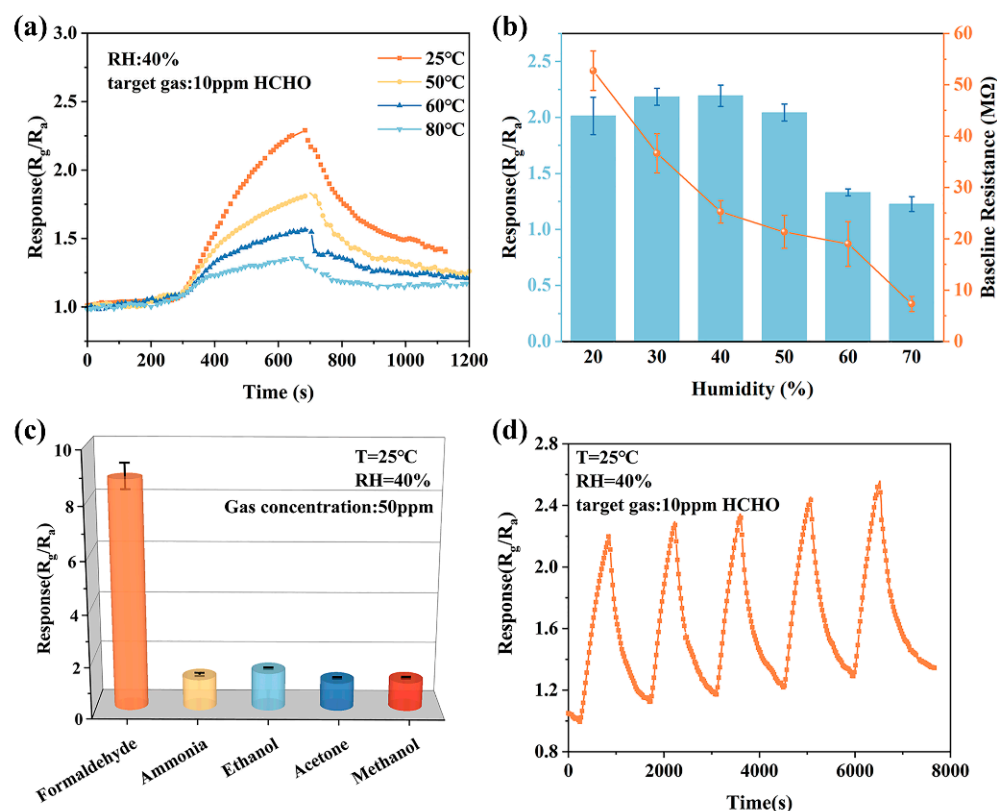


Figure 8. (a) The response of the MXene/NiO-P2 sensor to 10 ppm HCHO at different operating temperatures. (b) The response values and baseline resistances of the MXene/NiO-P2 sensor at different humidities. (c) Selectivity of the MXene/NiO-P2 sensor to HCHO and other VOCs gases, such as ammonia, ethanol, acetone, and methanol, with a concentration of 50 ppm at 25 °C. (d) The repeatability of the MXene/NiO-P2 sensor to 10 ppm HCHO during the five testing cycles at 25 °C.

The influence of relative humidity on the sensing properties of the HCHO sensor based on MXene/NiO-P2 was also studied, and is shown in Figure 8b. It can be seen that the baseline resistance of the sensor decreases with the increase in humidity from 20% to 70%. This may be due to the fact that the adsorption of water molecules on the sensing materials can improve the hole concentration of the p-type material by annihilating electrons from the material, resulting in a decrease in material resistance [44]. However, the response value of the sensor can remain relatively stable when the relative humidity is below 50%. As the relative humidity was over 50%, the response showed an obvious downward trend with the increase in the humidity. The phenomenon that higher humidity inhibits sensing performance can be explained by the following two reasons: First of all, when the humidity exceeds a certain level, the adsorption of water molecules will compete for the active sites on the sensor surface with HCHO molecules—the higher the humidity, the more active sites are occupied by water molecules. Secondly, HCHO is more easily soluble in water, and high humidity will lead to a decrease in the effective concentration of HCHO [45].

The selectivity and repeatability properties of the MXene/NiO-P2-based sensor are shown in Figure 8c,d, respectively. Figure 8c shows the response of the MXene/NiO-P2 sensor to 50 ppm formaldehyde, ammonia, ethanol, acetone, and methanol gas, indicating a good selectivity to formaldehyde gas. In a real environment with multiple gas components, it is very important to realize the interference-free detection of formaldehyde gas. As reported in the literature, a sensing array is an efficient means by which to realize detection in a mixed gas environment. Therefore, to construct the sensor array whilst including the prepared formaldehyde sensor and the gas sensors with a high response to other gases such as ammonia, ethanol, acetone, and methanol is worth studying [46–51]. The response curve of the MXene/NiO-P2 sensor to 10 ppm HCHO at room temperature were tested for five cycles, and the result is shown in Figure 8d. It can be noticed that the sensor based on MXene/NiO-P2 showed good repeatability. Furthermore, it should be mentioned that the change in the response base line in Figure 8a,d should be related to the long recovery time of the sensor. In the test cycle that was conducted in a short time, the resistance of the sensor could not recover to the initial state—such a result can also be found in a previous report [52].

The sensing response to 10 ppm HCHO was measured every 7 days for 9 consecutive measurements for a total of 56 days, as is shown in Figure 9. The response value can always be maintained around 2.29, with a fluctuation of no more than 10%, indicating that the sensor based on MXene/NiO-P2 had a good long-term stability. Furthermore, the response baseline not being able recover to the initial state is also related to the long recovery time of the sensor. Table 1 presents a comparison of the sensing performance of the MXene/NiO-P2-based chemiresistive-type sensor in this work with the previously reported HCHO sensor [53–57]. It can be seen that the MXene/NiO-P2-based sensor not only can work at room temperature, but can also display a higher response value and lower detection limit to HCHO gas.

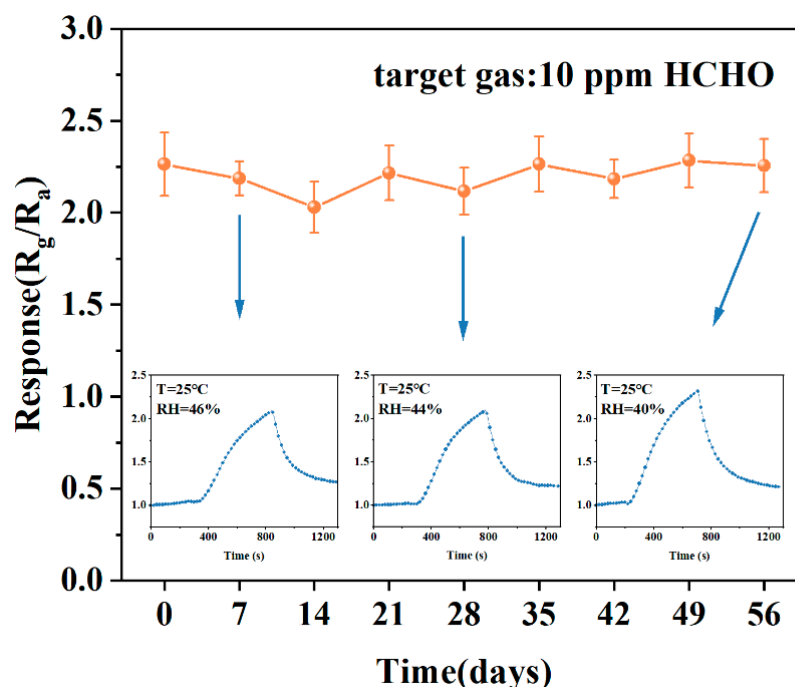


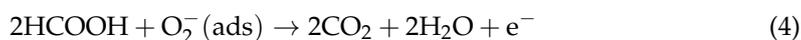
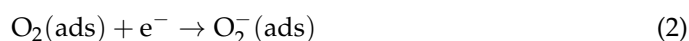
Figure 9. Long-term stability of the MXene/NiO-P2 sensor to 10 ppm HCHO for about 56 days at 25 °C.

Table 1. Comparison of the performance of the sensors proposed in this work with previously reported sensors for HCHO detection.

Sensing Material	Temperature (°C)	Response	LOD (ppm)	Ref.
NiO/NiFe ₂ O ₄ composite	240	17.5 (50 ppm)	0.1	[22]
NiO 3D flower	200	3.5 (100 ppm)	10	[23]
Pt/NiO	200	5.6 (300 ppm)	50	[53]
NiO Nanosheets	240	2.1 (50 ppm)	0.1	[54]
SnO ₂ /Ti ₃ C ₂ T _x MXene	160	38.6 (20 ppm)	0.05	[55]
ZnSnO ₃ /MXene	RT	62.4% (5 ppm)	5	[56]
In ₂ O ₃ /Ti ₃ C ₂ T _x MXene/Au	RT	31% (5 ppm)	5	[57]
Ti ₃ C ₂ T _x MXene/rGO/SnO ₂	RT	54.97% (10 ppm)	10	[19]
MXene/NiO	RT	8.8 (50 ppm)	1	This Work

3.3. Gas-Sensing Mechanism

As discussed above, the MXene/NiO material, in this work, displayed a typical p-type semiconductor characteristic. The sensing mechanism mainly corresponded with the adsorption and desorption reactions of the gas molecules on the surface of the sensor. Once the sensor was exposed to air, the oxygen molecules in the air were adsorbed on the surface via a capturing of the electrons from the conduction band of the sensing materials, resulting in chemisorbed oxygen. Since the MXene/NiO-based chemiresistive-type sensor was operated at a room temperature, O₂[−] was the predominant adsorbed oxygen species [58,59]. The adsorption process is shown in Equation (2) and the left part of Figure 10a. Due to the decrease in the electron concentration, the MXene/NiO sensor displayed a lower resistance in air. When the sensor was exposed to HCHO gas, the HCHO molecules reacted with the adsorbed oxygen, as is shown in Equations (3) and (4), and which were verified later by the in situ FTIR spectra. As shown in the right part of Figure 10a, the captured electrons were re-injected into the conduction band of the sensing material, thus reducing the hole concentration and increasing the resistance of the sensor [60]. With the gradual progress of the reaction, the surface-active site of the composite was almost completely occupied by HCHO, and the sensor resistance tended to a stable maximum, so as to produce an obvious sensing signal for HCHO.



Therefore, according to the above sensing processes, for the MXene/NiO-based sensor, the excellent sensing performance was understood to be mainly due to the formation of heterojunctions between MXene and NiO [61]. As shown in Figure 10b, the band gap of MXene and NiO were about 1.14 eV and 3.6 eV, respectively, and the work functions were 4.79 eV and 5.5 eV, respectively [62,63]. Since the work function of MXene was lower than that of the NiO nanoparticles, the electrons in the conduction band of MXene moved to the NiO, and the holes in the valence band of NiO transferred to MXene, thus forming a hole accumulation layer on the side of the MXene and a hole depletion layer on the side of the NiO (Figure 10c). The charge transfer between MXene and NiO leads to an increase in free electron concentration in the NiO material, which can enhance the adsorption of oxygen molecules (Equation (2)), thus further promoting the occurrence of Equations (3) and (4). More oxygen molecules and HCHO molecules taking part in the sensing reaction will cause the MXene/NiO sensor to produce a larger resistance change in air and in HCHO atmospheres, such that the MXene/NiO sensor can display a higher response signal to HCHO gas.

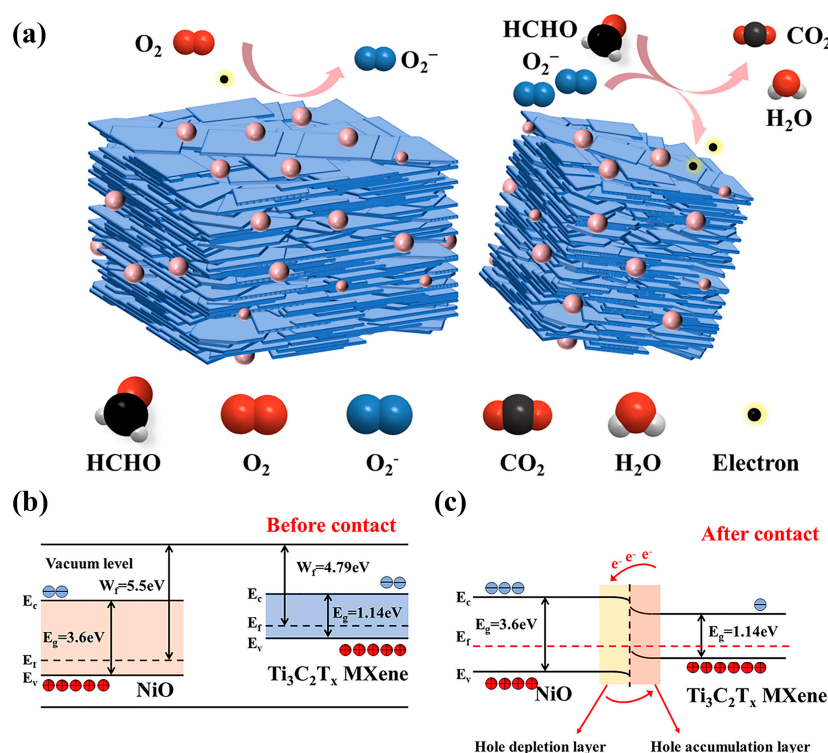


Figure 10. (a) Illustration of gas adsorption on the surface of the MXene/NiO material. (b,c) Energy band diagram of the MXene/NiO heterojunction before and after contact.

Furthermore, the high sensing performance of the MXene/NiO sensor was also related to the special structural characteristics of the MXene materials. Firstly, the MXene material contains abundant surface functional groups, such as OH⁻, F⁻, and some oxygen-containing functional groups, which can provide some growth locations for NiO nanoparticles [13,64]. As shown in Figure 3a, the signal intensity of F⁻ was reduced in the MXene/NiO-P2 material. Secondly, the MXene has a layered structure with a high specific surface area. The NiO nanoparticles were dispersed on the surface and the interlayer of the MXene materials, as is shown in Figure 1b, thereby providing more surface-active sites for HCHO adsorption. Therefore, more HCHO can be attracted to the interface region of the MXene/NiO heterojunction, which releases electrons, thus making the change in sensor resistance high enough to significantly improve the response at room temperature.

To further verify the transient intermediates and final products generated on the surface of the MXene/NiO-P2 composites during the HCHO adsorption process, the in situ FTIR of the sensor was measured, which is of great significance for exploring the sensing mechanism. Figure 11 shows the in situ FTIR of the MXene/NiO-P2 sensor in HCHO for 0 min, 1 min, 2 min, 5 min, and 10 min. The peaks at 1050 cm⁻¹ and 1150 cm⁻¹ corresponded to the C-O functional groups of the MXene material [65]. As the increase in exposure time occurred in the MXene/NiO-P2 in HCHO gas, the formation of some new substances can also be observed in Figure 11. The new peaks at 1352 cm⁻¹ and 1413 cm⁻¹ belong to molecularly adsorbed HCHO on the sensing material [66,67]. The peaks positioned at 1340 cm⁻¹ and 1557 cm⁻¹ correspond to the COO⁻ symmetric stretching and asymmetric stretching vibrations of formate species, respectively [68,69]. The peak centered around 1510 cm⁻¹ belongs to the vibrations of formate species. The above results indicate that the formate species is an intermediate product during the HCHO adsorption process. The peaks at 1620 cm⁻¹ and 1641 cm⁻¹ were attributed to the water molecules produced in reactions (3) and (4), while the peaks at 2343 cm⁻¹ and 2360 cm⁻¹ were associated with the CO₂ species, confirming the production of CO₂ in Equation (4) [70].

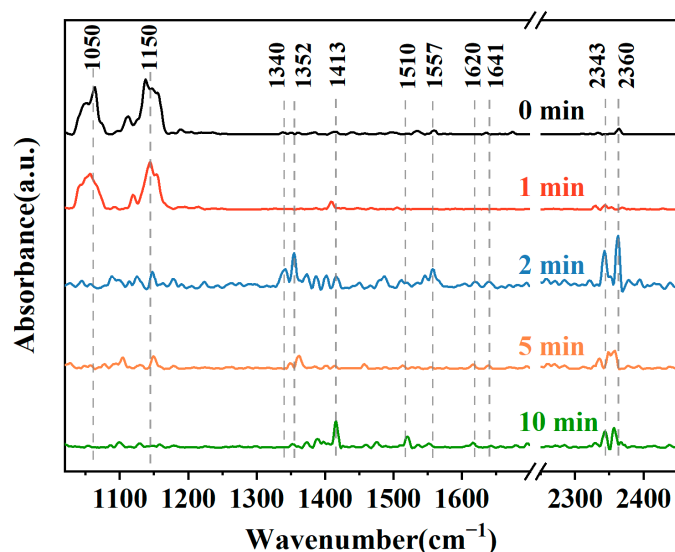


Figure 11. In situ FTIR spectra of the MXene/NiO-P2 sensor exposed to HCHO.

4. Conclusions

The MXene/NiO composites were prepared by an in situ precipitation strategy. The chemiresistive-type sensor based on MXene/NiO-P2 composites showed good selectivity, long term stability, and a higher response to HCHO compared with the pure MXene and pure NiO materials at room temperature. When the MXene/NiO-P2 sensor was exposed to 100 ppm HCHO, the gas sensing response was as high as 16.31. The LOD of the MXene/NiO-P2 sensor for HCHO was 1 ppm, which needs to be further improved in future work. The effective methods include modifying the prepared sensing material with noble metals (Au, Pt, Pd, etc.) and TiO₂ (which has an excellent sensing performance with respect to formaldehyde gas, as well as to UV irradiation). Furthermore, the influences of temperature and humidity on HCHO detection were also investigated. The experimental results showed that the sensor based on MXene/NiO-P2 material had good application prospects in HCHO monitoring at room temperatures. The high sensing performance of the MXene/NiO-P2 sensor for HCHO gas can be attributed to the formation of the heterojunctions between MXene and NiO, as well as due to the excellent structural properties of MXene.

Supplementary Materials: The following supporting information can be downloaded at: <https://www.mdpi.com/article/10.3390/chemosensors11040258/s1>. Figure S1. (a) Schematic illustration of the synthesis process of the sensing material. (b) Schematic diagram and photograph of the gas sensor. (c) Schematic diagram of the static testing system; Figure S2. SEM images of (a,b) MXene/NiO-P1 and (c,d) MXene/NiO-P3; Figure S3. Real-time resistance changes in the sensors based on (a) MXene/NiO-P1 and (b) MXene/NiO-P3 to 10–100 ppm HCHO at 25 °C and RH = 40%; Figure S4. Response changes in the sensors based on MXene/NiO-P2 and MXene-350C to 10–100 ppm HCHO at 25 °C and RH = 40%.

Author Contributions: Conceptualization, B.H., X.T., X.L., M.N.R. and J.P.; methodology, X.T., B.H., X.Z., M.N.R. and J.P.; data collection and analysis, X.T., B.H., X.L., X.Z. and Q.F.; validation, X.Z., Q.F., M.N.R. and J.P.; investigation, B.H., X.T., X.L., X.Z. and Q.F.; resources, X.L., B.H., Q.F. and M.N.R.; writing—original draft preparation, B.H., X.T., X.Z. and Q.F.; writing—review and editing, B.H. and X.L.; supervision, B.H., X.L. and J.P.; funding acquisition, X.L., B.H., Q.F. and M.N.R. All authors have read and agreed to the published version of the manuscript.

Funding: The authors highly appreciate the financial support received from the National Key R&D Program of China (No. 2021YFB3201302), the National Natural Science Foundation of China (No. 61971085, 62201117, and 62111530055), the Russian Foundation for Basic Research (No. 21-53-53018), the Fundamental Research Funds for the Central Universities (No. DUT19RC(3)054), and the Natural Science Foundation of Shandong Province (No. ZR2021MF081). This work was also supported by the Opening Project of Key Laboratory of Microelectronic Devices & Integrated Technology, Institute of Microelectronics, Chinese Academy of Sciences.

Institutional Review Board Statement: Not applicable.

Informed Consent Statement: Not applicable.

Data Availability Statement: Not applicable.

Acknowledgments: Special thanks are given to Sheikh A. Akbar from the Department of Materials Science and Engineering at Ohio State University for his kind assistance in improving the English proficiency of the article.

Conflicts of Interest: The authors declare no conflict of interest.

References

1. Wang, Z.; Zhang, R.; Gu, F.; Han, D. Facile synthesis of In₂O₃ nanoparticles with high response to formaldehyde at low temperature. *Int. J. Appl. Ceram. Technol.* **2019**, *16*, 1570–1580. [[CrossRef](#)]
2. Luecken, D.J.; Napelenok, S.L.; Strum, M.; Scheffe, R.; Phillips, S. Sensitivity of ambient atmospheric formaldehyde and ozone to precursor species and source types across the United States. *Environ. Sci. Technol.* **2018**, *52*, 4668–4675. [[CrossRef](#)]
3. Salthammer, T. The formaldehyde dilemma. *Int. J. Hyg. Environ. Health* **2015**, *218*, 433–436. [[CrossRef](#)] [[PubMed](#)]
4. Xingxing, F.; Yang, P.; Xiao, X.; Zhou, D.; Huang, R.; Zhang, X.; Cao, F.; Xiong, J.; Hu, Y.; Tu, Y. Ultra-fast and highly selective room-temperature formaldehyde gas sensing of Pt-decorated MoO₃ nanobelts. *J. Alloys Compd.* **2019**, *797*, 666–675.
5. Wu, J.; Feng, S.; Wei, X.; Shen, J.; Lu, W.; Shi, H.; Tao, K.; Lu, S.; Sun, T.; Yu, L. Facile synthesis of 3D graphene flowers for ultrasensitive and highly reversible gas sensing. *Adv. Funct. Mater.* **2016**, *26*, 7462–7469. [[CrossRef](#)]
6. Feng, Q.; Li, X.; Wang, J.; Gaskov, A.M. Reduced graphene oxide (rGO) encapsulated Co₃O₄ composite nanofibers for highly selective ammonia sensors. *Sens. Actuators B Chem.* **2016**, *222*, 864–870. [[CrossRef](#)]
7. Cho, S.Y.; Lee, Y.; Koh, H.J.; Jung, H.; Kim, J.S.; Yoo, H.W.; Kim, J.; Jung, H.T. Superior chemical sensing performance of black phosphorus: Comparison with MoS₂ and graphene. *Adv. Mater.* **2016**, *28*, 7020–7028. [[CrossRef](#)]
8. Cho, S.-Y.; Kim, S.J.; Lee, Y.; Kim, J.-S.; Jung, W.-B.; Yoo, H.-W.; Kim, J.; Jung, H.-T. Highly enhanced gas adsorption properties in vertically aligned MoS₂ layers. *ACS Nano* **2015**, *9*, 9314–9321. [[CrossRef](#)]
9. Wu, M.; He, M.; Hu, Q.; Wu, Q.; Sun, G.; Xie, L.; Zhang, Z.; Zhu, Z.; Zhou, A. Ti₃C₂ MXene-based sensors with high selectivity for NH₃ detection at room temperature. *ACS Sens.* **2019**, *4*, 2763–2770. [[CrossRef](#)]
10. Anasori, B.; Lukatskaya, M.R.; Gogotsi, Y. 2D metal carbides and nitrides (MXenes) for energy storage. *Nat. Rev. Mater.* **2017**, *2*, 16098. [[CrossRef](#)]
11. Hantanasirisakul, K.; Gogotsi, Y. Electronic and optical properties of 2D transition metal carbides and nitrides (MXenes). *Adv. Mater.* **2018**, *30*, 1804779. [[CrossRef](#)] [[PubMed](#)]
12. Yuan, W.; Yang, K.; Peng, H.; Li, F.; Yin, F. A flexible VOCs sensor based on a 3D Mxene framework with a high sensing performance. *J. Mater. Chem. A* **2018**, *6*, 18116–18124. [[CrossRef](#)]
13. Kim, S.J.; Koh, H.-J.; Ren, C.E.; Kwon, O.; Maleski, K.; Cho, S.-Y.; Anasori, B.; Kim, C.-K.; Choi, Y.-K.; Kim, J. Metallic Ti₃C₂T_x MXene gas sensors with ultrahigh signal-to-noise ratio. *ACS Nano* **2018**, *12*, 986–993. [[CrossRef](#)]
14. Zhang, D.; Mi, Q.; Wang, D.; Li, T. MXene/Co₃O₄ composite based formaldehyde sensor driven by ZnO/MXene nanowire arrays piezoelectric nanogenerator. *Sens. Actuators B Chem.* **2021**, *339*, 129923. [[CrossRef](#)]
15. Xue, Q.; Zhang, H.; Zhu, M.; Pei, Z.; Li, H.; Wang, Z.; Huang, Y.; Huang, Y.; Deng, Q.; Zhou, J. Photoluminescent Ti₃C₂ MXene quantum dots for multicolor cellular imaging. *Adv. Mater.* **2017**, *29*, 1604847. [[CrossRef](#)] [[PubMed](#)]
16. Lee, E.; VahidMohammadi, A.; Prorok, B.C.; Yoon, Y.S.; Beidaghi, M.; Kim, D.-J. Room temperature gas sensing of two-dimensional titanium carbide (MXene). *ACS Appl. Mater. Interfaces* **2017**, *9*, 37184–37190. [[CrossRef](#)]
17. He, T.; Liu, W.; Lv, T.; Ma, M.; Liu, Z.; Vasiliev, A.; Li, X. MXene/SnO₂ heterojunction based chemical gas sensors. *Sens. Actuators B Chem.* **2021**, *329*, 129275. [[CrossRef](#)]
18. Wang, Z.; Wang, F.; Hermawan, A.; Asakura, Y.; Hasegawa, T.; Kumagai, H.; Kato, H.; Kakihana, M.; Zhu, J.; Yin, S. SnO-SnO₂ modified two-dimensional MXene Ti₃C₂T_x for acetone gas sensor working at room temperature. *J. Mater. Sci. Technol.* **2021**, *73*, 128–138. [[CrossRef](#)]
19. Liu, M.; Song, P.; Liang, D.; Ding, Y.; Wang, Q. 3D porous Ti₃C₂T_x MXene/rGO/SnO₂ aerogel for formaldehyde detection at room temperature. *J. Alloys Compd.* **2022**, *925*, 166664. [[CrossRef](#)]
20. San, X.; Zhao, G.; Wang, G.; Shen, Y.; Meng, D.; Zhang, Y.; Meng, F. Assembly of 3D flower-like NiO hierarchical architectures by 2D nanosheets: Synthesis and their sensing properties to formaldehyde. *RSC Adv.* **2017**, *7*, 3540–3549. [[CrossRef](#)]

21. Lai, X.; Shen, G.; Xue, P.; Yan, B.; Wang, H.; Li, P.; Xia, W.; Fang, J. Ordered mesoporous NiO with thin pore walls and its enhanced sensing performance for formaldehyde. *Nanoscale* **2015**, *7*, 4005–4012. [[CrossRef](#)] [[PubMed](#)]
22. Xu, Y.; Tian, X.; Fan, Y.; Sun, Y. A formaldehyde gas sensor with improved gas response and sub-ppm level detection limit based on NiO/NiFe₂O₄ composite nanotetrahedrons. *Sens. Actuators B Chem.* **2020**, *309*, 127719. [[CrossRef](#)]
23. Hu, Q.; Wang, Z.; Chang, J.; Wan, P.; Huang, J.; Feng, L. Design and preparation of hollow NiO sphere-polyaniline composite for NH₃ gas sensing at room temperature. *Sens. Actuators B Chem.* **2021**, *344*, 130179. [[CrossRef](#)]
24. Peng, C.; Yang, X.; Li, Y.; Yu, H.; Wang, H.; Peng, F. Hybrids of two-dimensional Ti₃C₂ and TiO₂ exposing {001} facets toward enhanced photocatalytic activity. *ACS Appl. Mater. Interfaces* **2016**, *8*, 6051–6060. [[CrossRef](#)] [[PubMed](#)]
25. Hermawan, A.; Zhang, B.; Taufik, A.; Asakura, Y.; Hasegawa, T.; Zhu, J.; Shi, P.; Yin, S. CuO nanoparticles/Ti₃C₂T_x MXene hybrid nanocomposites for detection of toluene gas. *ACS Appl. Nano Mater.* **2020**, *3*, 4755–4766. [[CrossRef](#)]
26. Xiu, L.; Wang, Z.; Yu, M.; Wu, X.; Qiu, J. Aggregation-resistant 3D MXene-based architecture as efficient bifunctional electrocatalyst for overall water splitting. *ACS Nano* **2018**, *12*, 8017–8028. [[CrossRef](#)]
27. Ghidui, M.; Lukatskaya, M.R.; Zhao, M.-Q.; Gogotsi, Y.; Barsoum, M.W. Conductive two-dimensional titanium carbide ‘clay’ with high volumetric capacitance. *Nature* **2014**, *516*, 78–81. [[CrossRef](#)]
28. Liang, L.; Han, G.; Li, Y.; Zhao, B.; Zhou, B.; Feng, Y.; Ma, J.; Wang, Y.; Zhang, R.; Liu, C. Promising Ti₃C₂T_x MXene/Ni chain hybrid with excellent electromagnetic wave absorption and shielding capacity. *ACS Appl. Mater. Interfaces* **2019**, *11*, 25399–25409. [[CrossRef](#)]
29. Tian, K.; Wang, X.-X.; Li, H.-Y.; Nadimicherla, R.; Guo, X. Lotus pollen derived 3-dimensional hierarchically porous NiO microspheres for NO₂ gas sensing. *Sens. Actuators B Chem.* **2016**, *227*, 554–560. [[CrossRef](#)]
30. Zhang, C.; Qian, L.; Zhang, K.; Yuan, S.; Xiao, J.; Wang, S. Hierarchical porous Ni/NiO core–shells with superior conductivity for electrochemical pseudo-capacitors and glucose sensors. *J. Mater. Chem. A* **2015**, *3*, 10519–10525. [[CrossRef](#)]
31. Halim, J.; Cook, K.M.; Naguib, M.; Eklund, P.; Gogotsi, Y.; Rosen, J.; Barsoum, M.W. X-ray photoelectron spectroscopy of select multi-layered transition metal carbides (MXenes). *Appl. Surf. Sci.* **2016**, *362*, 406–417. [[CrossRef](#)]
32. Ren, Y.; Li, Y.; Wu, X.; Wang, J.; Zhang, G. S-scheme Sb₂WO₆/g-C₃N₄ photocatalysts with enhanced visible-light-induced photocatalytic NO oxidation performance. *Chin. J. Catal.* **2021**, *42*, 69–77. [[CrossRef](#)]
33. Wang, Z.; Jiang, L.; Wang, K.; Li, Y.; Zhang, G. Novel AgI/BiSbO₄ heterojunction for efficient photocatalytic degradation of organic pollutants under visible light: Interfacial electron transfer pathway, DFT calculation and degradation mechanism study. *J. Hazard. Mater.* **2021**, *410*, 124948. [[CrossRef](#)] [[PubMed](#)]
34. Liu, Z.; He, T.; Sun, H.; Huang, B.; Li, X. Layered MXene heterostructured with In₂O₃ nanoparticles for ammonia sensors at room temperature. *Sens. Actuators B Chem.* **2022**, *365*, 131918. [[CrossRef](#)]
35. Xu, S.; Wei, G.; Li, J.; Ji, Y.; Klyui, N.; Izotov, V.; Han, W. Binder-free Ti₃C₂T_x MXene electrode film for supercapacitor produced by electrophoretic deposition method. *Chem. Eng. J.* **2017**, *317*, 1026–1036. [[CrossRef](#)]
36. Xu, H.; Zheng, D.; Liu, F.; Li, W.; Lin, J. Synthesis of an MXene/polyaniline composite with excellent electrochemical properties. *J. Mater. Chem. A* **2020**, *8*, 5853–5858. [[CrossRef](#)]
37. He, T.; Sun, S.; Huang, B.; Li, X. MXene/SnS₂ Heterojunction for Detecting Sub-ppm NH₃ at Room Temperature. *ACS Appl. Mater. Interfaces* **2023**, *15*, 4194–4207. [[CrossRef](#)]
38. Bodurov, G.; Stefchev, P.; Ivanova, T.; Gesheva, K. Investigation of electrodeposited NiO films as electrochromic material for counter electrodes in “Smart Windows”. *Mater. Lett.* **2014**, *117*, 270–272. [[CrossRef](#)]
39. Zheng, Y.; Wang, J.; Yao, P. Formaldehyde sensing properties of electrospun NiO-doped SnO₂ nanofibers. *Sens. Actuators B Chem.* **2011**, *156*, 723–730. [[CrossRef](#)]
40. Zhang, S.; Zhao, L.; Huang, B.; Li, X. Enhanced sensing performance of Au-decorated TiO₂ nanospheres with hollow structure for formaldehyde detection at room temperature. *Sens. Actuators B Chem.* **2022**, *358*, 131465. [[CrossRef](#)]
41. Zhang, S.; Zhao, L.; Huang, B.; Li, X. UV-activated formaldehyde sensing properties of hollow TiO₂@SnO₂ heterojunctions at room temperature. *Sens. Actuators B Chem.* **2020**, *319*, 128264. [[CrossRef](#)]
42. Liu, L.; Li, X.; Dutta, P.K.; Wang, J. Room temperature impedance spectroscopy-based sensing of formaldehyde with porous TiO₂ under UV illumination. *Sens. Actuators B Chem.* **2013**, *185*, 1–9. [[CrossRef](#)]
43. Liu, M.; Wang, Z.; Song, P.; Yang, Z.; Wang, Q. Flexible MXene/rGO/CuO hybrid aerogels for high performance acetone sensing at room temperature. *Sens. Actuators B Chem.* **2021**, *340*, 129946. [[CrossRef](#)]
44. Wang, Y.; Zhou, Y.; Wang, Y. Humidity activated ionic-conduction formaldehyde sensing of reduced graphene oxide decorated nitrogen-doped MXene/titanium dioxide composite film. *Sens. Actuators B Chem.* **2020**, *323*, 128695. [[CrossRef](#)]
45. Guo, C.; Dong, X.; Zhang, X.; Cheng, X.; Li, Q.; Sun, Y.; Liu, W.; Huo, L.; Xu, Y. Controllable construction of Ho₂O₃ nanomaterials with different dimensions (1D, 2D, and 3D) for real-time monitoring human breathing and body surface humidity detection. *J. Mater. Chem. A* **2021**, *9*, 11632–11640. [[CrossRef](#)]
46. Zhang, J.; Xue, Y.; Sun, Q.; Zhang, T.; Chen, Y.; Yu, W.; Xiong, Y.; Wei, X.; Yu, G.; Wan, H. A miniaturized electronic nose with artificial neural network for anti-interference detection of mixed indoor hazardous gases. *Sens. Actuators B Chem.* **2021**, *326*, 128822. [[CrossRef](#)]
47. Albert, K.J.; Lewis, N.S.; Schauer, C.L.; Sotzing, G.A.; Stitzel, S.E.; Vaid, T.P.; Walt, D.R. Cross-reactive chemical sensor arrays. *Chem. Rev.* **2000**, *100*, 2595–2626. [[CrossRef](#)]

48. Li, X.; Chen, N.; Lin, S.; Wang, J.; Zhang, J. NiO-wrapped mesoporous TiO₂ microspheres based selective ammonia sensor at room temperature. *Sens. Actuators B Chem.* **2015**, *209*, 729–734. [[CrossRef](#)]
49. Wang, Z.; Tian, Z.; Han, D.; Gu, F. Highly sensitive and selective ethanol sensor fabricated with In-doped 3DOM ZnO. *ACS Appl. Mater. Interfaces* **2016**, *8*, 5466–5474. [[CrossRef](#)]
50. Qi, Q.; Zhang, T.; Liu, L.; Zheng, X.; Yu, Q.; Zeng, Y.; Yang, H. Selective acetone sensor based on dumbbell-like ZnO with rapid response and recovery. *Sens. Actuators B Chem.* **2008**, *134*, 166–170. [[CrossRef](#)]
51. Acharyya, D.; Huang, K.Y.; Chattopadhyay, P.P.; Ho, M.S.; Fecht, H.J.; Bhattacharyya, P. Hybrid 3D structures of ZnO nanoflowers and PdO nanoparticles as a highly selective methanol sensor. *Analyst* **2016**, *141*, 2977–2989. [[CrossRef](#)] [[PubMed](#)]
52. Kuang, D.; Guo, X.; Zhu, Z.; Ding, Y.; Sun, X.; Wu, Z.; Zhang, L.; Zhou, Y.; He, Y. Enhanced room temperature ammonia response of 2D-Ti₃C₂T_x MXene decorated with Ni(OH)₂ nanoparticles. *Ceram. Int.* **2021**, *47*, 19471–19480. [[CrossRef](#)]
53. Dong, C.; Li, Q.; Chen, G.; Xiao, X.; Wang, Y. Enhanced formaldehyde sensing performance of 3D hierarchical porous structure Pt-functionalized NiO via a facile solution combustion synthesis. *Sens. Actuators B Chem.* **2015**, *220*, 171–179. [[CrossRef](#)]
54. Li, G.; Wang, X.; Ding, H.; Zhang, T. A facile synthesis method for Ni(OH)₂ ultrathin nanosheets and their conversion to porous NiO nanosheets used for formaldehyde sensing. *Rsc Adv.* **2012**, *2*, 13018–13023. [[CrossRef](#)]
55. Niu, G.; Zhang, M.; Wu, B.; Zhuang, Y.; Ramachandran, R.; Zhao, C.; Wang, F. Nanocomposites of pre-oxidized Ti₃C₂T_x MXene and SnO₂ nanosheets for highly sensitive and stable formaldehyde gas sensor. *Ceram. Int.* **2023**, *49*, 2583–2590. [[CrossRef](#)]
56. Sima, Z.; Song, P.; Ding, Y.; Lu, Z.; Wang, Q. ZnSnO₃ nanocubes/Ti₃C₂T_x MXene composites for enhanced formaldehyde gas sensing properties at room temperature. *Appl. Surf. Sci.* **2022**, *598*, 153861. [[CrossRef](#)]
57. Liu, M.; Sun, R.; Sima, Z.; Song, P.; Ding, Y.; Wang, Q. Au-decorated In₂O₃ nanospheres/exfoliated Ti₃C₂T_x MXene nanosheets for highly sensitive formaldehyde gas sensing at room temperature. *Appl. Surf. Sci.* **2022**, *605*, 154839. [[CrossRef](#)]
58. Navaneethan, M.; Patil, V.L.; Ponnusamy, S.; Muthamizhchelvan, C.; Kawasaki, S.; Patil, P.S.; Hayakawa, Y. Sensitivity enhancement of ammonia gas sensor based on Ag/ZnO flower and nanoellipsoids at low temperature. *Sens. Actuators B Chem.* **2018**, *255*, 672–683.
59. Zhang, S.; Yang, M.; Liang, K.; Turak, A.; Zhang, B.; Meng, D.; Wang, C.; Qu, F.; Cheng, W.; Yang, M. An acetone gas sensor based on nanosized Pt-loaded Fe₂O₃ nanocubes. *Sens. Actuators B Chem.* **2019**, *290*, 59–67. [[CrossRef](#)]
60. Zhang, R.; Liu, X.; Zhou, T.; Zhang, T. Controllable construction of multishelled p-type cuprous oxide with enhanced formaldehyde sensing. *J. Colloid Interface Sci.* **2019**, *535*, 58–65. [[CrossRef](#)]
61. Miller, D.R.; Akbar, S.A.; Morris, P.A. Nanoscale metal oxide-based heterojunctions for gas sensing: A review. *Sens. Actuators B Chem.* **2014**, *204*, 250–272. [[CrossRef](#)]
62. Sun, B.; Lv, H.; Liu, Z.; Wang, J.; Bai, X.; Zhang, Y.; Chen, J.; Kan, K.; Shi, K. Co₃O₄@PEI/Ti₃C₂T_x MXene nanocomposites for a highly sensitive NO_x gas sensor with a low detection limit. *J. Mater. Chem. A* **2021**, *9*, 6335–6344. [[CrossRef](#)]
63. Greiner, M.T.; Helander, M.G.; Wang, Z.-B.; Tang, W.-M.; Lu, Z.-H. Effects of processing conditions on the work function and energy-level alignment of NiO thin films. *J. Phys. Chem. C* **2010**, *114*, 19777–19781. [[CrossRef](#)]
64. Sun, S.; Wang, M.; Chang, X.; Jiang, Y.; Zhang, D.; Wang, D.; Zhang, Y.; Lei, Y. W₁₈O₄₉/Ti₃C₂T_x MXene nanocomposites for highly sensitive acetone gas sensor with low detection limit. *Sens. Actuators B Chem.* **2020**, *304*, 127274. [[CrossRef](#)]
65. Wu, G.; Liu, Y.; He, Y.; Feng, J.; Li, D. Reaction pathway investigation using in situ Fourier transform infrared technique over Pt/CuO and Pt/TiO₂ for selective glycerol oxidation. *Appl. Catal. B Environ.* **2021**, *291*, 120061. [[CrossRef](#)]
66. Sun, S.; Ding, J.; Bao, J.; Gao, C.; Qi, Z.; Li, C. Photocatalytic oxidation of gaseous formaldehyde on TiO₂: An in situ DRIFTS study. *Catal. Lett.* **2010**, *137*, 239–246. [[CrossRef](#)]
67. Zhang, C.; He, H.; Tanaka, K.-I. Catalytic performance and mechanism of a Pt/TiO₂ catalyst for the oxidation of formaldehyde at room temperature. *Appl. Catal. B Environ.* **2006**, *65*, 37–43. [[CrossRef](#)]
68. Nasriddinov, A.; Platonov, V.; Garshev, A.; Rumyantseva, M. Low Temperature HCHO Detection by SnO₂/TiO₂@ Au and SnO₂/TiO₂@ Pt: Understanding by In-Situ DRIFT Spectroscopy. *Nanomaterials* **2021**, *11*, 2049. [[CrossRef](#)]
69. Sun, J.; Li, X.; Zhao, Q.; Liu, B. Ultrathin nanoflake-assembled hierarchical BiOBr microflower with highly exposed {001} facets for efficient photocatalytic degradation of gaseous ortho-dichlorobenzene. *Appl. Catal. B Environ.* **2021**, *281*, 119478. [[CrossRef](#)]
70. Aristizabal, B.H.; de Correa, C.M.; Serykh, A.I.; Hetrick, C.E.; Amiridis, M.D. In situ FTIR study of the adsorption and reaction of ortho-dichlorobenzene on Pd-Co sulfated zirconia catalysts. *J. Catal.* **2008**, *258*, 95–102. [[CrossRef](#)]

Disclaimer/Publisher's Note: The statements, opinions and data contained in all publications are solely those of the individual author(s) and contributor(s) and not of MDPI and/or the editor(s). MDPI and/or the editor(s) disclaim responsibility for any injury to people or property resulting from any ideas, methods, instructions or products referred to in the content.